Low-Resolution Editing is All You Need for High-Resolution Editing

Junsung Lee^{1*} Hyunsoo Lee^{1*} Yong Jae Lee³ Bohyung Han^{1,2}
¹ECE & ²IPAI, Seoul National University ³University of Wisconsin-Madison

{leejs0525, philip21, bhhan}@snu.ac.kr, yongjaelee@cs.wisc.edu



Figure 1. Generated images using the proposed method, ScaleEdit. Our method successfully generates high-resolution edited images by leveraging low-resolution editing results as reference images.

Abstract

High-resolution content creation is rapidly emerging as a central challenge in both the vision and graphics communities. While images serve as the most fundamental modality for visual expression, content generation that aligns with the user intent requires effective, controllable high-resolution image manipulation mechanisms. However, existing approaches remain limited to low-resolution settings, typically supporting only up to 1K resolution. In this work, we introduce the task of high-resolution image editing and propose a test-time optimization framework to address it. Our method performs patch-wise optimization on high-resolution source images, followed by a fine-grained detail transfer module and a novel synchronization strategy to maintain consistency across patches. Extensive experiments show that our method produces high-quality edits, facilitating the way toward highresolution content creation.

1. Introduction

High-resolution visual content has become essential in modern digital workflows, including image synthesis [10, 15, 20, 35, 56], video generation [3, 6, 19], document process-

ing [29], autonomous driving [53], and 3D shape generation [45, 46]. In such scenarios, users frequently seek precise and intentional modifications to an existing high-resolution image rather than generating a new one from scratch. Unlike naïve image generation, image manipulation preserves the identity and semantic layout of the source image, while allowing controlled adjustments that reflect the user's intention. Therefore, editing serves as a reliable strategy to produce user-controlled high-resolution content while preserving both structural integrity and visual fidelity. This motivates the need for editing methods that maintain finegrained texture details and structural consistency at high resolutions (e.g., > 1K $\approx 1024^2$).

We introduce the task of *high-resolution image editing*, where the objective is to modify a high-resolution source image according to a target visual concept while preserving its fine-grained details. However, existing image-to-image translation methods [14, 26, 58] operate at fixed low resolutions and cannot directly handle large-scale inputs. A simple solution is to perform editing at low resolution and subsequently apply super-resolution methods [7, 9, 11, 44], but this approach fails to recover micro-scale textures since the fine-grained details of the source image are not conditioned during the editing process. Thus, a novel strategy is required

^{*}indicates equal contribution.

to support editing in the high-resolution domain.

To address the task defined in our work, we propose ScaleEdit. Editing a high resolution image requires an optimization formulation that preserves both semantics and fine-grained details. This can be facilitated by leveraging the strong performance of existing low-resolution image editing methods [14, 26, 58]. Under this view, the central challenge of the task becomes clear: how to faithfully transfer the fine-scale details of the high-resolution source image into the edited result. Our intuition is that this objective can be achieved by exploiting the generative priors learned by pretrained diffusion models [13, 34, 37], which are known to produce perceptually plausible edits.

Concretely, our key idea is to transfer fine-grained details from the high-resolution source image to the target image by introducing a learnable transfer function defined in the intermediate feature space of a pretrained diffusion model. This transfer function operates as a learnable 1×1 convolution, enabling precise control over fine-grained detail transfer. However, diffusion models are trained at fixed input resolutions and cannot operate directly on high-resolution image setups. Thus, to fully inherit their strong generative priors while accommodating large-scale inputs, we adopt a patch-wise strategy, dividing the image into model-native resolution regions. This enables preserving micro-scale details while still benefiting from the strong priors encoded in the pretrained diffusion model. A novel patch synchronization mechanism is then applied to ensure global consistency across patches. We note that the proposed synchronization method does not require overlapping inference, effectively decreasing the computational demand of the overall method. We summarize our contributions as follows:

- To the best of our knowledge, our work is the first to propose the high-resolution image editing task, supported by our novel patch-wise inference mechanism that enables the use of strong generative priors in the high-resolution domain.
- We develop a feature-space transfer function and a synchronization strategy across non-overlapping patches to perform high-resolution editing in a test-time optimization manner.
- Experimental results demonstrate that the proposed method achieves state-of-the-art editing capacity that enable diverse instruction-based editing.

2. Related works

Text-driven image editing. Text-conditional image editing methods inherit the strong generative capabilities of diffusion models [13, 23, 37, 39]. Building on these priors, a broad set of U-Net-based [38] approaches [2, 4, 5, 8, 12, 16, 21, 24, 25, 31, 47] achieve strong performance across diverse scenarios through latent optimization, attention manipulation, and instruction-based control.

More recently, transformer-based [48] diffusion models have further advanced editing capabilities. For example, Step1X-Edit [26] presents general-purpose instruction-based image editing framework by coupling a multimodal LLM with a DiT-based [33] decoder trained on a large-scale, taxonomy-driven editing dataset. ICEdit [57] leverages the in-context generation capability of large DiT models, treating edits as a diptych-style prompts and only requires lightweight LoRA-MoE fine-tuning [18]. KV-Edit [58] enables training-free editing by reusing cached key-value tokens under a user-provided mask, which is an idea inspired by LLM's KV-cache mechanisms [54], to preserve background pixels while effectively modifying the foreground regions. However, while these methods can edit images only up to 1K resolution, our approach leverages the generative priors of existing methods to enable editing even at 2K and higher resolutions.

Diffusion-based super-resolution. Real-World Image Super Resolution (Real-ISR) seeks to reconstruct detailed highresolution images from low-resolution inputs that exhibit diverse and unknown degradations. With the rapid advancement of diffusion models, diffusion-based approaches have increasingly been adopted for tackling this task. Prior methods [1, 7, 9, 11, 44, 49–52, 55] built on large text-to-image models have recently shown strong performance. TSD-SR [9] distills a multi-step text-to-image diffusion model into an one-step super-resolution network via target score distillation and a distribution-aware sampling. PiSA-SR [44] introduces dual LoRA [18] modules separately dedicated to pixel-level regression and semantic-level enhancement. On the other hand, DiT-SR [7] introduces a diffusion transformer [33] trained from scratch with a U-shaped multiscale design and frequency-aware timestep conditioning. DiT4SR [11] adapts the Stable Diffusion v3 [13] architecture by injecting low-resolution features directly into the transformer [48] blocks via bidirectional attention and convolution. While existing SR methods rely on training to generate high-resolution outputs, the proposed method restores fine details through test-time optimization without any model training.

3. Preliminary

Diffusion models. Diffusion models [17, 40–42] demonstrate remarkable ability in synthesizing versatile content across multiple modalities. Starting from an initial noise latent $\mathbf{x}_T \sim \mathcal{N}(\mathbf{0}, \mathbf{I})$, they generate a trajectory of latent variables $\{\mathbf{x}_t^{\text{rev}}\}_{t=T}^0$ through a reverse diffusion process. DDIM [41] formulates this reverse process as a deterministic procedure. Specifically, $\mathbf{x}_{t-1}^{\text{rev}}$ is sampled from $\mathbf{x}_t^{\text{rev}}$ as:

$$\mathbf{x}_{t-1}^{\text{rev}} = f^{\text{rev}}(\mathbf{x}_{t}^{\text{rev}}, t)$$

$$= \sqrt{\alpha_{t-1}} \hat{\mathbf{x}}_{0}(\mathbf{x}_{t}^{\text{rev}}, t) + \sqrt{1 - \alpha_{t-1}} \epsilon_{\theta}(\mathbf{x}_{t}^{\text{rev}}, t) \quad (1)$$

where $\{\alpha_t\}_{t=0}^T$ is the predefined decreasing variance schedule, $\epsilon_{\theta}(\cdot, \cdot)$ denotes the noise prediction network, and $\hat{\mathbf{x}}_0(\mathbf{x}_t, t)$ is the estimated Tweedie at timestep t, computed using Tweedie's Formula [43] given by

$$\hat{\mathbf{x}}_0(\mathbf{x}_t, t) = \frac{\mathbf{x}_t - \sqrt{1 - \alpha_t} \epsilon_{\theta}(\mathbf{x}_t, t)}{\sqrt{\alpha_t}}.$$
 (2)

Iteratively applying Eq. (1) gives a clean sample x_0 .

Image-to-image translation. In diffusion-based image-to-image translation [5, 31, 47], the deterministic forward and reverse processes [41] are commonly employed to reconstruct a given source image. Starting from a source image \mathbf{x}_0 , the forward process introduces noise according to

$$\mathbf{x}_{t+1}^{\text{fwd}} = f^{\text{fwd}}(\mathbf{x}_{t}^{\text{fwd}}, t)$$

$$= \sqrt{\alpha_{t+1}} \hat{\mathbf{x}}_{0}(\mathbf{x}_{t}^{\text{fwd}}, t) + \sqrt{1 - \alpha_{t+1}} \epsilon_{\theta}(\mathbf{x}_{t}^{\text{fwd}}, t), \quad (3)$$

and iterative application of Eq. (3) for T times yield the noised source latent $\mathbf{x}_T^{\mathrm{fwd}}$. The reconstruction of the source image is then obtained by applying the reverse DDIM process (Eq. (1)) from $\mathbf{x}_T^{\mathrm{rev}} = \mathbf{x}_T^{\mathrm{fwd}}$, producing $\mathbf{x}_0^{\mathrm{recon}}$. Under the assumption of negligible discretization error [42], then this forward–reconstruction procedure is theoretically lossless, guaranteeing $\mathbf{x}_0 = \mathbf{x}_0^{\mathrm{recon}}$.

Null-text inversion. In practice, discretization errors can accumulate during the forward process, leading to imperfect reconstructions. To account for such deviations, Null-text inversion [28] refines the reverse process (Eq. (1)) by introducing a timestep-dependent parameter ϕ_t , which serves as a learnable unconditional embedding. The parameter ϕ_t is optimized to align the reverse trajectory with the forward trajectory by minimizing the discrepancy between their corresponding latents:

$$\min_{\phi_t} \|\mathbf{x}_{t-1}^{\text{fwd}} - f^{\text{rev}}(\tilde{\mathbf{x}}_t^{\text{rev}}, t, \phi_t)\|_2^2, \tag{4}$$

where $\tilde{\mathbf{x}}_t^{\mathrm{rev}}$ denotes the latent obtained from the optimized reverse process. This strategy enables accurate reconstruction of the source image.

4. ScaleEdit

4.1. Problem formulation

We consider three conditioning images: (1) the high-resolution source $I_{\mathrm{src}}^{\mathrm{high}} \in \mathbb{R}^{H_h \times W_h \times 3}$, (2) its downsampled version $I_{\mathrm{src}}^{\mathrm{low}} \in \mathbb{R}^{H_l \times W_l \times 3}$, (3) and a low-resolution reference $I_{\mathrm{ref}}^{\mathrm{low}} \in \mathbb{R}^{H_l \times W_l \times 3}$ that represents the desired target image. The image $I_{\mathrm{src}}^{\mathrm{low}}$ is obtained by downsampling $I_{\mathrm{src}}^{\mathrm{high}}$, and the reference $I_{\mathrm{ref}}^{\mathrm{low}}$ is produced by applying a standard low-resolution image editing method (e.g., [14]) to $I_{\mathrm{src}}^{\mathrm{low}}$. The

objective is to generate a high-resolution edited output $I_{\rm ref}^{\rm high}$ that reflects the overall semantics of $I_{\rm ref}^{\rm low}$ while maintaining the fine-grained details present in $I_{\rm src}^{\rm high}$. This formulation enables us to leverage the strong priors and reliable editing behavior of existing low-resolution diffusion models.

4.2. Overview

The proposed method generates high-resolution output $I_{\rm ref}^{\rm high}$ in a patch-wise manner, for precise control of the fine-grained details present in $I_{\rm src}^{\rm high}$. We first divide all conditioning images into $N\times M$ patches. For each patch, we transfer the fine-grained details residing in $I_{\rm src}^{\rm high}$ by manipulating the intermediate features of a pretrained diffusion model (Sec. 4.4), producing $N\times M$ enhanced target patches. Then, they are synchronized and fused into a coherent high-resolution target image (Sec. 4.5), ensuring smoothness across patch boundaries. Figure 2 provides a summary of our method.

4.3. Patch-wise diffusion trajectory extraction

Given three conditioning images, we first resize the low-resolution source $I_{\rm src}^{\rm low}$ and reference image $I_{\rm ref}^{\rm low}$ to match the resolution of the high-resolution source $I_{\rm src}^{\rm high}$. We then divide each image into non-overlapping $N\times M$ patches of size $\mathbb{R}^{H_d\times W_d\times 3}$, where $H_d\times W_d$ corresponds to the input resolution of the pretrained diffusion model [23, 37]. Thus, $N=H_h/H_d$ and $M=W_h/W_d$, resulting in a total of $N\times M$ patches. We denote the $i^{\rm th}$ patch of $I_{\rm src}^{\rm high}$ as $I_{\rm src}^{\rm high}[i]$, and we define $I_{\rm src}^{\rm low}[i]$ and $I_{\rm ref}^{\rm low}[i]$ likewise.

Each patch is then encoded using a VAE [22] encoder. Here, we define the resulting latent representations of the high-resolution source, low-resolution source, and reference patches as $\mathbf{x}_0^{\text{high}}[i]$, $\mathbf{x}_0^{\text{low}}[i]$, and $\mathbf{y}_0^{\text{low}}[i]$, respectively, where $1 \leq i \leq NM$. We subsequently apply the forward process, optionally enhanced with Null-text inversion [28], to obtain their diffusion trajectories, which are given by

$$\{\mathbf{x}_{t}^{\text{high}}[i]\}_{t=0}^{T}, \{\mathbf{x}_{t}^{\text{low}}[i]\}_{t=0}^{T}, \{\mathbf{y}_{t}^{\text{low}}[i]\}_{t=0}^{T}.$$
 (5)

4.4. Detail enhancement module

To inject fine-grained details from a low-resolution image to a target high-resolution image, we introduce a transfer function that aligns the diffusion trajectories of the low-resolution into high-resolution domains. Specifically, starting from $\tilde{\mathbf{x}}_T[i] = \mathbf{x}_T^{\text{low}}[i]$, we aim to guide its reverse diffusion trajectory $\{\tilde{\mathbf{x}}_t[i]\}_{t=0}^T$ to follow that of the high-resolution source latent $\{\mathbf{x}_t^{\text{high}}[i]\}_{t=0}^T$.

To accomplish this, we define a timestep-dependent transfer function $\phi(i,t)$ that adjusts the intermediate feature representation $\mathbf{h}_t[i]$ of the pretrained diffusion model. Here, $\mathbf{h}_t[i]$ denotes the output of the ResNet block along the upward path of the U-Net architecture [38], or the output of the final linear layer following the single-stream block in

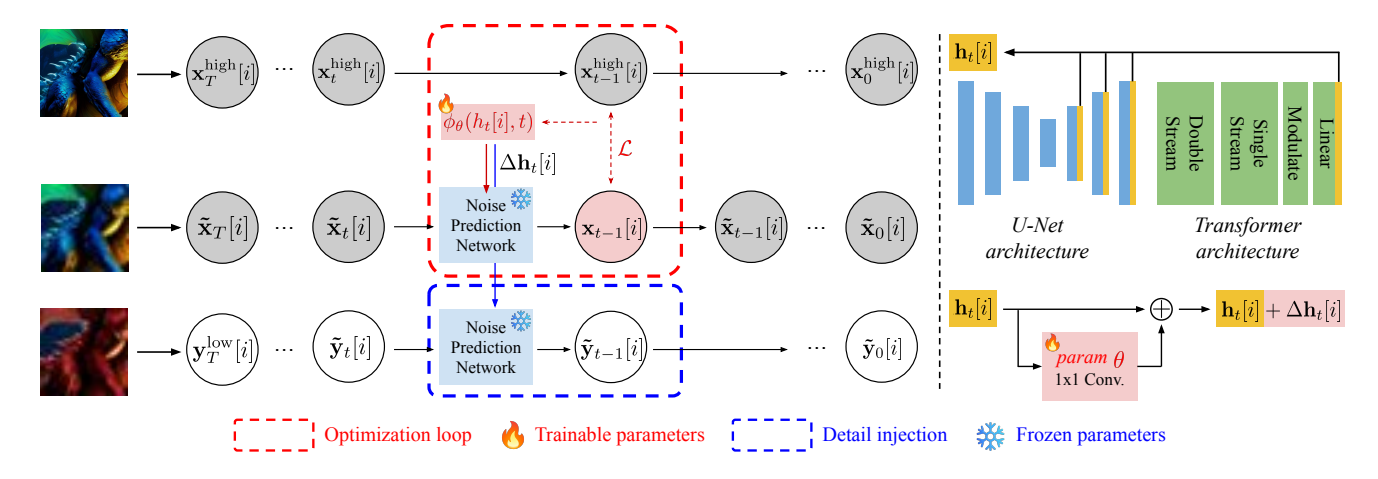


Figure 2. Overview of the proposed method. (Left) We first optimize the transfer function $\phi_{\theta}(\mathbf{h}_{i}[t],t)$ to capture fine-grained details encoded in the high-resolution source trajectory $\{\mathbf{x}_{t}^{\text{high}}[i]\}_{t=0}^{T}$. We then apply the optimized transfer function during the reverse process of $\{\tilde{\mathbf{y}}_{t}[i]\}_{t=0}^{T}$, yielding a detail-enhance latent $\tilde{\mathbf{y}}_{0}[i] = \mathbf{y}_{0}^{\text{high}}[i]$. (Right) We illustrate how the transfer function modulates the intermediate feature within the diffusion model.

Transformer-based architectures [23]. This is illustrated as the yellow sub-block on the right side of Figure 2, and a detailed discussion of the layer selection strategy is explained in the Appendix. We then introduce a feature modification term $\Delta \mathbf{h}_t[i] = \phi(i,t)$, which is applied to manipulate the intermediate feature of the pretrained model [23, 37] at each timestep t. The transfer function is optimized to align the low-resolution trajectory with the high-resolution trajectory by minimizing the following training objective:

$$\mathcal{L} := ||\mathbf{x}_{t-1}^{\text{high}}[i] - f^{\text{rev}}(\tilde{\mathbf{x}}_t[i], t; \Delta \mathbf{h}_t[i])||_2^2, \tag{6}$$

where $f^{\mathrm{rev}}(\cdot, \cdot \mid \Delta \mathbf{h}_t[i])$ is the reverse diffusion process function with the manipulated intermediate feature of $\mathbf{h}_t[i] + \Delta \mathbf{h}_t[i]$:

$$f^{\text{rev}}(\mathbf{x}_{t}^{\text{rev}}, t; \Delta \mathbf{h}_{t}[i]) := \sqrt{\alpha_{t-1}} \hat{\mathbf{x}}_{0}(\mathbf{x}_{t}^{\text{rev}}, t; \Delta \mathbf{h}_{t}[i])$$
(7)
$$+ \sqrt{1 - \alpha_{t-1}} \epsilon_{\theta}(\mathbf{x}_{t}^{\text{rev}}, t; \Delta \mathbf{h}_{t}[i]).$$

Note that $f^{\text{rev}}(\mathbf{x}_t^{\text{rev}}, t)$ in Eq. 1 equals to $f^{\text{rev}}(\mathbf{x}_t^{\text{rev}}, t; \mathbf{0})$.

A straightforward parameterization of the timestep-dependent transfer function is to use a learnable constant vector $\phi(i,t) = \mathbf{c}_t[i]$, resulting in the adjusted intermediate feature $\mathbf{h}_t[i] + \mathbf{c}_t[i]$. However, we observe that it fails to produce reliable transformations, especially when the source and reference differ in semantics, e.g., cat-to-dog. We hypothesize that this limitation is caused since a single global constant vector may not be suitable to model varying degrees of change throughout the edited image and thus cannot adapt to varying spatial structures.

To overcome this issue, we instead formulate the transfer function as an operation adaptive to $\mathbf{h}_t[i]$, rather than as a global constant vector. That is, we design the feature modification term as

$$\Delta \mathbf{h}_t[i] := \phi_\theta(\mathbf{h}_t[i], t), \tag{8}$$

where θ is the trainable parameter that defines the operation for each timestep t. Empirically, we define the transfer function using a 1×1 convolution applied to $\mathbf{h}_t[i]$, i.e. $\mathrm{conv}_{1\times 1}(\mathbf{h}_t[i])$. This lightweight operation allows feature mixing across channels while preserving spatial layout, which turns out to be effective for transferring fine-grained details in a spatially adaptive manner.

After optimizing the transfer function, we inject it during the reverse process to generate the target image, starting from $\tilde{\mathbf{y}}_T[i] = \mathbf{y}_T^{\text{low}}[i]$ and resulting in a trajectory of $\{\tilde{\mathbf{y}}_t[i]\}_{t=0}^T$, where $\tilde{\mathbf{y}}_{t-1}[i]$ is sampled via

$$\tilde{\mathbf{y}}_{t-1}[i] = f^{\text{rev}}(\tilde{\mathbf{y}}_t[i], t; \Delta \mathbf{h}_t[i]). \tag{9}$$

Then, we finally take $\mathbf{y}_0^{\text{high}}[i] = \mathbf{\tilde{y}}_0[i]$. This sampling strategy is effective since the objective in Eq. (6) encourages the transfer function to act as a feature-level detail injection operator, guiding the low-resolution source trajectory toward the high-resolution source trajectory while preserving the fine-grained details.

Optimizing and injecting $\Delta \mathbf{h}_t[i]$ over all timesteps facilitates fine-detail transfer, but may gradually distort the content of the source image and yield higher computation. In contrast, limiting optimization to only early timesteps preserves the source image's content but may under-transfer fine details. To handle this trade-off, we introduce a hyperparameter τ that denotes the latest timestep at which our transfer function optimization is applied; that is, $\Delta \mathbf{h}_t[i] = \mathbf{0}, \ \forall t \geq \tau$. Thus, it serves as a flexible controller that balances the level of detail transfer relative to content preservation, further allowing one to choose the trade-off depending on the editing strength and desired fidelity.

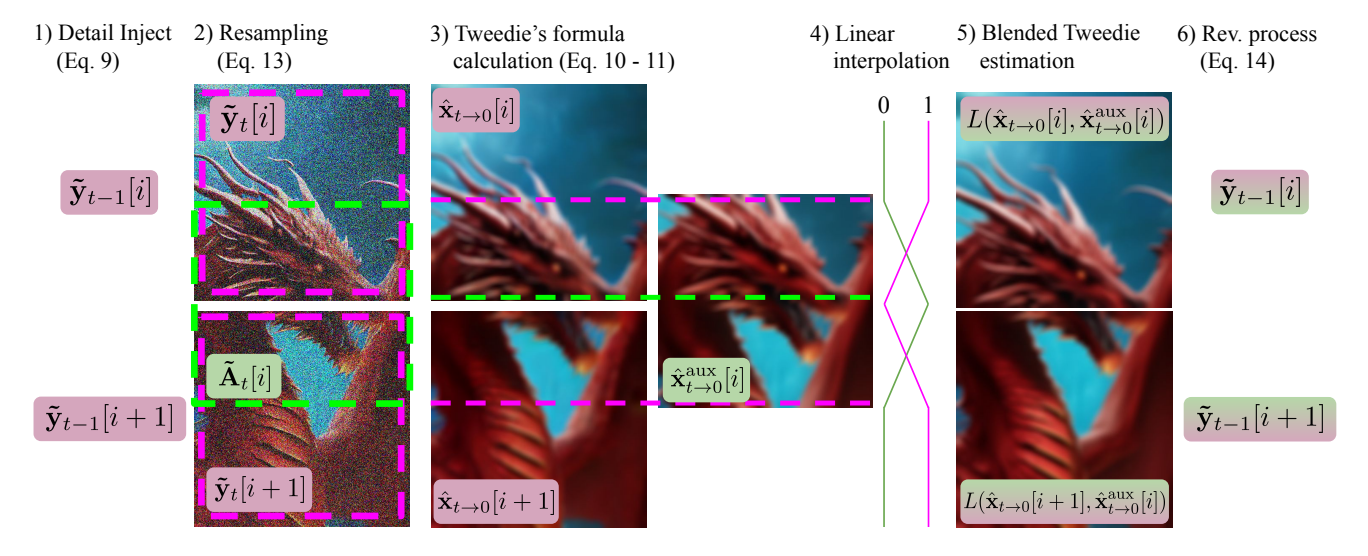


Figure 3. Overview of the synchronization strategy. Starting from the detail enhancement process (Eq. (9)), we perform resampling (Eq. (13)) and compute the blended Tweedie estimate. This estimate is then used to synchronize adjacent patches during the reverse process (Eq. (14)).

4.5. Synchronization between patches

While the transfer function $\Delta \mathbf{h}_t[i]$ injects fine-grained details into each patch, applying it per patch independently may lead to inconsistent textures and visible artifacts at patch boundaries. To ensure global coherence across patches, we introduce a synchronization mechanism that combines blended Tweedie updates (Sec. 4.5.1) with a resampling strategy (Sec. 4.5.2). For clarity, we describe the case that the adjacent patches are vertically aligned, namely $\tilde{\mathbf{y}}_t[i]$ and $\tilde{\mathbf{y}}_t[i+1]$. The same procedure applies equivalently when they are placed along the horizontal directions.

4.5.1. Blended-tweedie-based updates

To synchronize adjacent patches, we introduce an auxiliary latent $\tilde{\mathbf{A}}_t[i,i+1]$, constructed by spatially blending the bottom half of $\tilde{\mathbf{y}}_t[i]$ and the upper half of $\tilde{\mathbf{y}}_t[i+1]$ at timestep t. Since each patch is denoised independently, their latent trajectories may diverge, often producing visible discontinuities along their boundary. However, $\tilde{\mathbf{A}}_t[i,i+1]$ contains the boundary region, and therefore its Tweedie estimate may naturally captures a smoother transition between the two patches. By blending the Tweedie estimate of an auxiliary patch with those of the original patches, the boundary between neighboring patches becomes more coherent, reducing artifacts and enhancing spatial continuity.

For the spatial blending, we first apply Eq. (2) to obtain the original patches' Tweedie estimates:

$$\hat{\mathbf{x}}_{t\to 0}^{\text{aux}}[i, i+1] = \hat{\mathbf{x}}_0(\tilde{\mathbf{A}}_t[i, i+1], t)$$
 (10)

$$\hat{\mathbf{x}}_{t\to 0}[i] = \hat{\mathbf{x}}_0(\tilde{\mathbf{y}}_t[i], t). \tag{11}$$

Then we define $L(\hat{\mathbf{x}}_{t\to 0}[i], \hat{\mathbf{x}}_{t\to 0}^{\mathrm{aux}}[i, i+1])$, a blended Tweedie estimate that is used to swap the $\hat{\mathbf{x}}_0$ term in Eq. (1)

during the reverse process of $\tilde{\mathbf{y}}_t[i]$. Let W_p and H_p denote the patch width and height, respectively. We linearly interpolate the bottom half of $\tilde{\mathbf{y}}_t[i]$ and the corresponding region of the auxiliary latent $\tilde{\mathbf{A}}_t[i,i+1]$, i.e. the top half of $\tilde{\mathbf{A}}_t[i,i+1]$, whose overlap has spatial size $H_p/2 \times W_p$. To achieve this, we define a vertical interpolation weight as:

$$\mathbf{M}(v,t) = \frac{2v}{H_p} \cdot \left(1 - \frac{t}{\tau}\right) \quad 0 \le v \le H_p/2, \tag{12}$$

which increases linearly from the boundary toward the center of the overlap, so that the contribution of the auxiliary latent grows smoothly across the overlapping region. We then substitute the bottom half of the Tweedie estimate for $\tilde{\mathbf{y}}_t[i]$ with the linearly interpolated one, while keeping its top half unchanged. This yields the blended Tweedie estimate with respect to $\hat{\mathbf{x}}_{t\to 0}[i]$ and $\hat{\mathbf{x}}_{t\to 0}^{\mathrm{aux}}[i,i+1]$.

For the adjacent patch $\tilde{\mathbf{y}}_t[i+1]$, we apply the vertically mirrored blend operation. Specifically, we compute $L(\hat{\mathbf{x}}_{t\to 0}[i+1], \hat{\mathbf{x}}_{t\to 0}^{\mathrm{aux}}[i,i+1])$ with the weight of $1-\mathbf{M}$ (vertically reversed ramp). Detailed formulas indicating these blending strategies are described in the Appendix. This blending ensures spatial smoothness between adjacent patches.

4.5.2. Resampling strategy

A challenge in the above formulation is that $\Delta \mathbf{h}_t$ remains undefined for $\tilde{\mathbf{A}}_t[i,i+1]$, since adjacent patches $\tilde{\mathbf{y}}_t[i]$ and $\tilde{\mathbf{y}}_t[i+1]$ contain independently injected detail terms, $\Delta \mathbf{h}_t[i]$ and $\Delta \mathbf{h}_t[i+1]$. In principle, $\Delta \mathbf{h}_t$ for $\tilde{\mathbf{A}}_t[i,i+1]$ can be computed explicitly; however, this entails a costly additional optimization loop. So instead, we propose an alternative approach which we refer to as the *resampling strategy*, where synchronization is decoupled from detail injection. The key

Table 1. Quantitative evaluation under 1K- and 2K-editing scenarios using the pretrained Stable Diffusion [37]. We compare the proposed method with diffusion-based super-resolution methods [7, 9, 11, 44]. Our method shows superior performance compared to the baselines.

Method	1K-Editing				2K-Editing			
	HaarPSI [36]	M-MSE	M-SSIM	M-PSNR	HaarPSI [36]	M-MSE	M-SSIM	M-PSNR
DiT-SR [7]	0.335	0.058	0.695	21.519	0.316	0.057	0.754	21.379
DiT4SR [11]	0.324	0.060	0.625	20.740	0.305	0.058	0.684	20.701
PiSA-SR [44]	0.328	0.058	0.668	21.273	0.312	0.056	0.755	21.320
TSD-SR [9]	0.329	0.061	0.649	20.765	0.312	0.059	0.715	20.795
ScaleEdit (Ours)	0.342	0.054	0.739	22.114	0.331	0.053	0.805	21.955

idea is to reconstruct latents that preserve the fine-grained details already injected by the transfer function, but without dependency on any explicit $\Delta \mathbf{h}_t$ term. This allows synchronization to proceed without defining a separate $\Delta \mathbf{h}_t$ for $\tilde{\mathbf{A}}_t[i,i+1]$.

Given the detail-injected latents $\tilde{\mathbf{y}}_{t-1}[i]$ and $\tilde{\mathbf{y}}_{t-1}[i+1]$ obtained via Eq. (9), we apply a DDIM forward step *without* re-injecting the transfer function:

$$\tilde{\mathbf{y}}_{t}^{\text{rsp}}[i] = f^{\text{fwd}}(\tilde{\mathbf{y}}_{t-1}[i], t-1),$$

$$\tilde{\mathbf{y}}_{t}^{\text{rsp}}[i+1] = f^{\text{fwd}}(\tilde{\mathbf{y}}_{t-1}[i+1], t-1). \tag{13}$$

This resampling process yields detail-preserving latents $\tilde{\mathbf{y}}_t^{\mathrm{rsp}}$ that eliminates the need to define $\Delta \mathbf{h}_t$ for the auxiliary latent $\tilde{\mathbf{A}}_t[i,i+1]$. Using these resampled latents, we compute the blended Tweedie estimate using the synchronization procedure described in Sec. 4.5.1. Finally, the actual reverse process at timestep t is performed through Eq. (14):

$$\tilde{\mathbf{y}}_{t-1}[i] = \sqrt{\alpha_{t-1}} L(\hat{\mathbf{x}}_{t\to 0}[i], \hat{\mathbf{x}}_{t\to 0}^{\mathrm{aux}}[i]) + \sqrt{1 - \alpha_{t-1}} \epsilon_{\theta}(\tilde{\mathbf{y}}_{t}^{\mathrm{rsp}}[i], t).$$
(14)

The proposed mechanism harmonizes patch-wise diffusion trajectories, yielding globally consistent synthesis with fewer boundary artifacts and preserved fine-grained details.

5. Experiments

5.1. Implementation details

We implement our method based on the official codebase of Null-text inversion [28] using PyTorch [32]. We test our method primarily on the Stable Diffusion [37] v2.1-base model and we also show that our method is applicable to the transformer-based [48] FLUX.1-dev [23] model. Note that we provide the implementation details for applying our method to the FLUX model in the Appendix. For both cases, we use a total timestep of T=50 and set hyperparameter $\tau=15$. During the forward and reverse diffusion process, we use an empty prompt (""). We adopt Null-text inversion as the default for the experiments using Stable Diffusion to achieve accurate reconstruction. After obtaining $N\times M$ latents $\{\mathbf{y}_0^{\text{high}}[i]\}_{i=1}^{NM}$, we spatially merge them and decode the resulting latent using the VAE [22] decoder to get $I_{\text{ref}}^{\text{high}}$.

5.2. Data acquisition

Editing scenarios. To comprehensively evaluate high-resolution image editing, we consider two settings that reflect practical usage scenarios. We firstly examine the IK-editing scenario, where the reference and target resolutions are set to 512^2 and 1K, respectively. While existing diffusion-based editing methods [14] generally support editing up to this scale, we include this setting not as a challenging benchmark, but to highlight that our method transfers the fine-grained details faithfully. Next, we evaluate 2K-editing, which corresponds to a more common real-world setup for editing beyond the operating resolution of pretrained diffusion models.

Asset generation. We construct high-quality assets tailored for our task. We first generate a total of 4K resolution source images using FreeScale [35], then downsample them to 2K, 1K, and 512^2 resolution to obtain multi-resolution source images. Source prompts and editing instructions are produced with ChatGPT [30], where the instructions span four editing configurations: (1) two types of object replacement, (2) style transfer, and (3) background modification. We then apply NanoBanana [14] to the 512^2 and 1K versions of each source image to obtain the corresponding edited images. Here, the 512^2 -sized images serve as low-resolution references for 1K-editing, whereas the 1K resolution images serve as reference inputs for the 2K-editing scenario.

5.3. Quantitative evaluation

Baselines. A straightforward strategy for our task is to perform editing at a lower resolution and then apply superresolution (SR) methods. However, as discussed in the introduction, this approach fails to recover micro-scale textures because the fine-grained details of the source image are not conditioned during SR process. To verify that our claim is valid, we construct baselines by combining a state-of-the-art low-resolution editing method, NanoBanana [14], with various super-resolution approaches. Specifically, we compare against (1) DiT-SR [7], (2) DiT4SR [11], (3) PiSA-SR [44], and (4) TSD-SR [9]. We use a total of 400 (conditioning images, text instruction) pairs for evaluation.

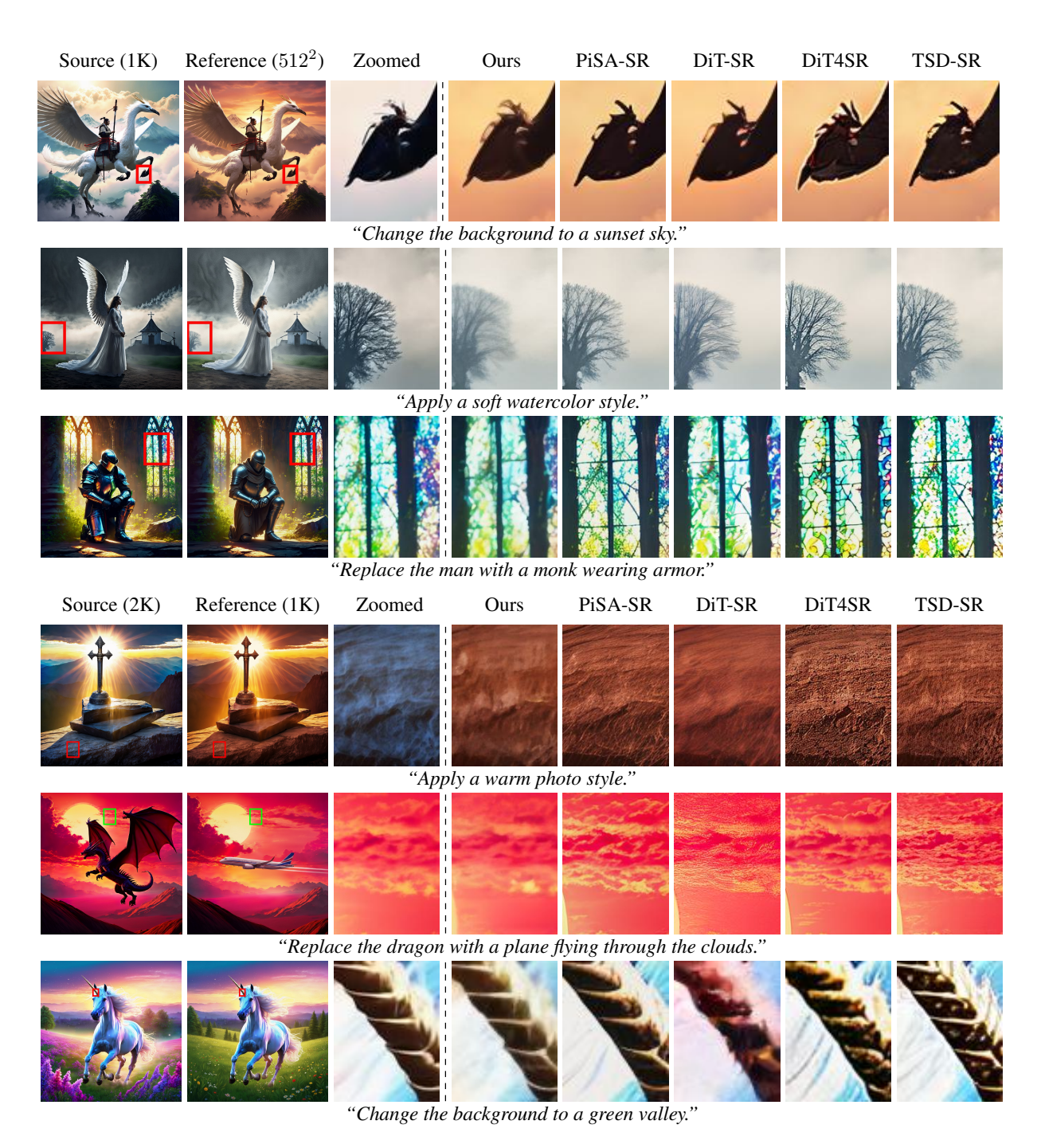


Figure 4. [Best visualized when magnified.] Qualitative comparison of the ScaleEdit with diffusion-based super-resolution baselines [7, 9, 11, 44]. First three rows show the results of 1K-editing, while the last three rows visualize 2K-editing scenario. Here, we use the pretrained Stable Diffusion [37] for ScaleEdit.

Metrics. We evaluate the results using four widely adapted metrics: MSE, SSIM, PSNR and HaarPSI [36]. To measure MSE, SSIM, and PSNR, we compute their masked variants by applying region-specific masks to the source and target images, which are denoted as M-MSE, M-SSIM, and M-PSNR, respectively. In particular, we use background

masks for object change tasks and foreground masks for background modification tasks. These masks are generated using LANG-SAM [27], which produces instruction-aware foreground and background segmentations. We emphasize that the masked metrics allow us to quantify how well each method preserves the regions of the source image that are

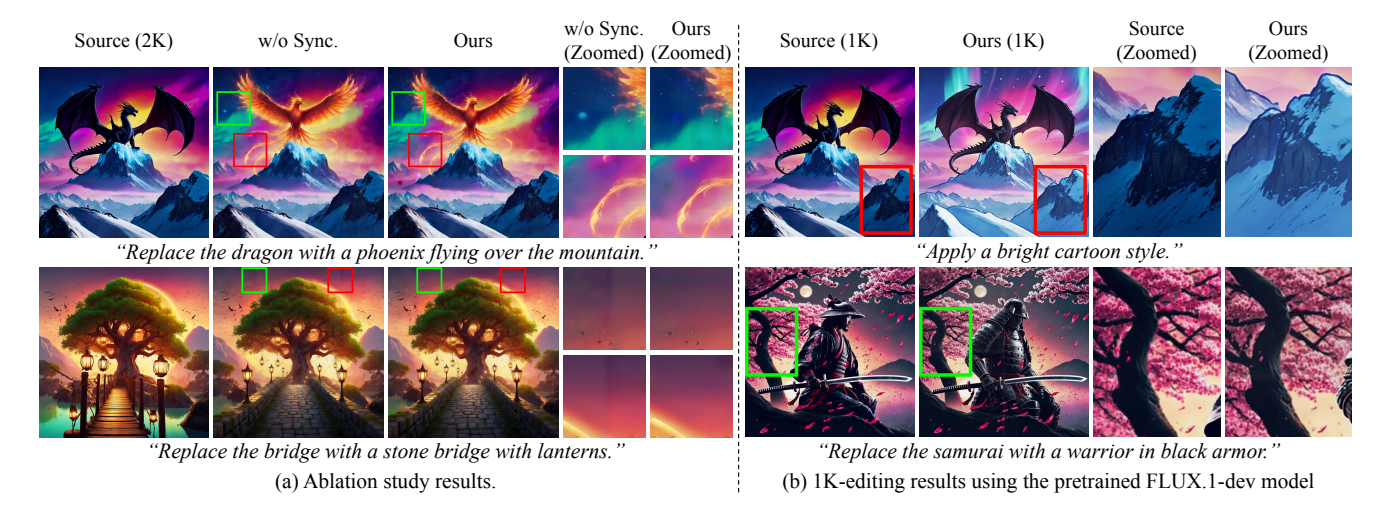


Figure 5. [Best visualized when magnified.] We visualize the effect of synchronization strategy in part (a), while we show the results of our method combined with the pretrained FLUX 1-dev [23] model in part (b).

intended to remain unchanged during editing. HaarPSI measures perceptual similarity in a wavelet-aware manner, allowing us to evaluate how effectively fine-grained details from the source image are transferred into the target image.

Comparisons. We quantitatively compare our method with baselines under both 1K-editing and 2K-editing scenarios. Table 1 summarizes the evaluation results. For each column of the table, we **bold** and <u>underline</u> the best and second-best result. As shown, our method consistently outperforms all baselines, highlighting the effectiveness of the detail enhancement and synchronization mechanism. In contrast, SR-based pipelines struggle to recover fine-grained details from the source image. Moreover, the superior performance of our approach on masked-variant metrics indicates that it synthesizes the target image in a more source-aware manner, mitigating the inherent limitations of SR-based methods that exhibits source-unconditional diffusion process.

5.4. Qualitative results

We present qualitative comparisons between our method and baseline approaches using the pretrained Stable Diffusion [37] in Figure 4. Here, the target image is expected to satisfy two criteria simultaneously: (1) accurately inherit the fine-grained details from the zoomed source image and (2) correctly reflect the semantics described in the text instruction. Our method produces superior results, faithfully transferring fine-grained details of the source image to the target image while leveraging the desired semantics from the text instructions. For example, in the 2nd row, the baselines struggle to adopt the "watercolor" style, whereas our method effectively renders the watercolor appearance while preserving the detail of the source image. Similarly, in the 4th and 6th rows, our approach reliably carries over the texture-like

details from the source, while the baselines exhibit noticeable color shifts or distorted textures. We also visualize additional qualitative results in Fig. 1 and 5 (right). Importantly, we emphasize that our method is not limited to Stable Diffusion architecture; it also generalizes to other backbones such as FLUX [23].

5.5. Ablation study

We show the effectiveness of the proposed patch-wise synchronization strategy through an ablation study. As illustrated in Figure 5 (left), the absence of synchronization leads to noticeable boundary artifacts, producing visible seams and inconsistencies along patch borders. In contrast, synchronization enforces coherent denoising trajectories across neighboring patches, resulting in artifact-free transitions while preserving the local fidelity of each patch.

6. Conclusion

We introduced the task of high-resolution image editing for the first time and proposed a general framework to address it. To fully inherit the strong prior of the pretrained image generation model, we divide the high-resolution source image into patches that match the model's native input resolution. We then transfer fine-grained details from the source to the target image through a learnable transfer function that operates on intermediate features of the pretrained network. To alleviate boundary artifacts between patches, we further presented a synchronization approach that eliminates the need for overlapping-view sampling used in prior synchronization methods, meaningfully reducing computational overhead. Experiments across multiple resolution editing scenarios demonstrated that our method is capable to high-resolution image editing.

References

- [1] Yuang Ai, Xiaoqiang Zhou, Huaibo Huang, Xiaotian Han, Zhengyu Chen, Quanzeng You, and Hongxia Yang. Dreamclear: High-capacity real-world image restoration with privacy-safe dataset curation. *NeurIPS*, 2024. 2
- [2] Omri Avrahami, Dani Lischinski, and Ohad Fried. Blended diffusion for text-driven editing of natural images. In CVPR, 2022. 2
- [3] Andreas Blattmann, Robin Rombach, Huan Ling, Tim Dockhorn, Seung Wook Kim, Sanja Fidler, and Karsten Kreis. Align your latents: High-resolution video synthesis with latent diffusion models. In CVPR, 2023. 1
- [4] Tim Brooks, Aleksander Holynski, and Alexei A Efros. Instructpix2pix: Learning to follow image editing instructions. In CVPR, 2023. 2
- [5] Mingdeng Cao, Xintao Wang, Zhongang Qi, Ying Shan, Xi-aohu Qie, and Yinqiang Zheng. Masactrl: Tuning-free mutual self-attention control for consistent image synthesis and editing. In *ICCV*, 2023. 2, 3
- [6] Junyu Chen, Wenkun He, Yuchao Gu, Yuyang Zhao, Jincheng Yu, Junsong Chen, Dongyun Zou, Yujun Lin, Zhekai Zhang, Muyang Li, et al. Dc-videogen: Efficient video generation with deep compression video autoencoder. arXiv:2509.25182, 2025. 1
- [7] Kun Cheng, Lei Yu, Zhijun Tu, Xiao He, Liyu Chen, Yong Guo, Mingrui Zhu, Nannan Wang, Xinbo Gao, and Jie Hu. Effective diffusion transformer architecture for image superresolution. In AAAI, 2025. 1, 2, 6, 7
- [8] Guillaume Couairon, Jakob Verbeek, Holger Schwenk, and Matthieu Cord. Diffedit: Diffusion-based semantic image editing with mask guidance. *ICLR*, 2023. 2
- [9] Linwei Dong, Qingnan Fan, Yihong Guo, Zhonghao Wang, Qi Zhang, Jinwei Chen, Yawei Luo, and Changqing Zou. Tsd-sr: One-step diffusion with target score distillation for real-world image super-resolution. In CVPR, 2025. 1, 2, 6, 7
- [10] Ruoyi Du, Dongliang Chang, Timothy Hospedales, Yi-Zhe Song, and Zhanyu Ma. Demofusion: Democratising highresolution image generation with no \$\$\$. In CVPR, 2024.
- [11] Zheng-Peng Duan, Jiawei Zhang, Xin Jin, Ziheng Zhang, Zheng Xiong, Dongqing Zou, Jimmy Ren, Chun-Le Guo, and Chongyi Li. Dit4sr: Taming diffusion transformer for real-world image super-resolution. In *ICCV*, 2025. 1, 2, 6, 7
- [12] Dave Epstein, Allan Jabri, Ben Poole, Alexei Efros, and Aleksander Holynski. Diffusion self-guidance for controllable image generation. *NeurIPS*, 2023. 2
- [13] Patrick Esser, Sumith Kulal, Andreas Blattmann, Rahim Entezari, Jonas Müller, Harry Saini, Yam Levi, Dominik Lorenz, Axel Sauer, Frederic Boesel, et al. Scaling rectified flow transformers for high-resolution image synthesis. In *ICML*, 2024. 2
- [14] Google. Introducing Gemini 2.5 Flash Image, our state-of-the-art image model. https://developers.googleblog.com/en/introducing-gemini-2-5-flash-image/, 2025. Codename "Nano Banana". 1, 2, 3, 6, 12

- [15] Yingqing He, Shaoshu Yang, Haoxin Chen, Xiaodong Cun, Menghan Xia, Yong Zhang, Xintao Wang, Ran He, Qifeng Chen, and Ying Shan. Scalecrafter: Tuning-free higherresolution visual generation with diffusion models. In *ICLR*, 2024. 1
- [16] Amir Hertz, Ron Mokady, Jay Tenenbaum, Kfir Aberman, Yael Pritch, and Daniel Cohen-Or. Prompt-to-prompt image editing with cross attention control. *ICLR*, 2023. 2
- [17] Jonathan Ho, Ajay Jain, and Pieter Abbeel. Denoising diffusion probabilistic models. *NeurIPS*, 2020. 2
- [18] Edward J Hu, Yelong Shen, Phillip Wallis, Zeyuan Allen-Zhu, Yuanzhi Li, Shean Wang, Lu Wang, Weizhu Chen, et al. Lora: Low-rank adaptation of large language models. *ICLR*, 2022.
- [19] Teng Hu, Jiangning Zhang, Zihan Su, and Ran Yi. Ultragen: High-resolution video generation with hierarchical attention. arXiv:2510.18775, 2025.
- [20] Linjiang Huang, Rongyao Fang, Aiping Zhang, Guanglu Song, Si Liu, Yu Liu, and Hongsheng Li. Fouriscale: A frequency perspective on training-free high-resolution image synthesis. In ECCV, 2024. 1
- [21] Gwanghyun Kim, Taesung Kwon, and Jong Chul Ye. Diffusionclip: Text-guided diffusion models for robust image manipulation. In CVPR, 2022. 2
- [22] Diederik P Kingma and Max Welling. Auto-encoding variational bayes. arXiv:1312.6114, 2013. 3, 6, 11
- [23] Black Forest Labs. Flux. https://github.com/ black-forest-labs/flux, 2024. 2, 3, 4, 6, 8, 12
- [24] Hyunsoo Lee, Minsoo Kang, and Bohyung Han. Conditional score guidance for text-driven image-to-image translation. *NeurIPS*, 2023. 2
- [25] Junsung Lee, Minsoo Kang, and Bohyung Han. Diffusion-based image-to-image translation by noise correction via prompt interpolation. In ECCV, 2024. 2
- [26] Shiyu Liu, Yucheng Han, Peng Xing, Fukun Yin, Rui Wang, Wei Cheng, Jiaqi Liao, Yingming Wang, Honghao Fu, Chunrui Han, Guopeng Li, Yuang Peng, Quan Sun, Jingwei Wu, Yan Cai, Zheng Ge, Ranchen Ming, Lei Xia, Xianfang Zeng, Yibo Zhu, Binxing Jiao, Xiangyu Zhang, Gang Yu, and Daxin Jiang. Step1x-edit: A practical framework for general image editing. arXiv:2504.17761, 2025. 1, 2
- [27] Luca Medeiros. lang-segment-anything. https://github.com/luca-medeiros/lang-segment-anything, 2023. 7
- [28] Ron Mokady, Amir Hertz, Kfir Aberman, Yael Pritch, and Daniel Cohen-Or. Null-text inversion for editing real images using guided diffusion models. In CVPR, 2023. 3, 6
- [29] Junbo Niu, Zheng Liu, Zhuangcheng Gu, Bin Wang, Linke Ouyang, Zhiyuan Zhao, Tao Chu, Tianyao He, Fan Wu, Qintong Zhang, et al. Mineru2. 5: A decoupled visionlanguage model for efficient high-resolution document parsing. arXiv:2509.22186, 2025. 1
- [30] OpenAI. Gpt-5 technical report, 2025. https://openai.com/research/. 6
- [31] Gaurav Parmar, Krishna Kumar Singh, Richard Zhang, Yijun Li, Jingwan Lu, and Jun-Yan Zhu. Zero-shot image-to-image translation. In SIGGRAPH, 2023. 2, 3

- [32] Adam Paszke, Sam Gross, Francisco Massa, Adam Lerer, James Bradbury, Gregory Chanan, Trevor Killeen, Zeming Lin, Natalia Gimelshein, Luca Antiga, et al. Pytorch: An imperative style, high-performance deep learning library. NeurIPS, 2019. 6
- [33] William Peebles and Saining Xie. Scalable diffusion models with transformers. In ICCV, 2023. 2
- [34] Dustin Podell, Zion English, Kyle Lacey, Andreas Blattmann, Tim Dockhorn, Jonas Müller, Joe Penna, and Robin Rombach. Sdxl: Improving latent diffusion models for high-resolution image synthesis. *ICLR*, 2024. 2
- [35] Haonan Qiu, Shiwei Zhang, Yujie Wei, Ruihang Chu, Hangjie Yuan, Xiang Wang, Yingya Zhang, and Ziwei Liu. Freescale: Unleashing the resolution of diffusion models via tuning-free scale fusion. In *ICCV*, 2025. 1, 6, 12
- [36] Rafael Reisenhofer, Sebastian Bosse, Gitta Kutyniok, and Thomas Wiegand. A haar wavelet-based perceptual similarity index for image quality assessment. Signal Processing: Image Communication, 2018. 6, 7
- [37] Robin Rombach, Andreas Blattmann, Dominik Lorenz, Patrick Esser, and Björn Ommer. High-resolution image synthesis with latent diffusion models. In CVPR, 2022. 2, 3, 4, 6, 7, 8, 11, 12
- [38] Olaf Ronneberger, Philipp Fischer, and Thomas Brox. U-net: Convolutional networks for biomedical image segmentation. In *International Conference on Medical image computing and computer-assisted intervention*, 2015. 2, 3, 11
- [39] Chitwan Saharia, William Chan, Saurabh Saxena, Lala Li, Jay Whang, Emily L Denton, Kamyar Ghasemipour, Raphael Gontijo Lopes, Burcu Karagol Ayan, Tim Salimans, et al. Photorealistic text-to-image diffusion models with deep language understanding. NeurIPS, 2022. 2
- [40] Jascha Sohl-Dickstein, Eric Weiss, Niru Maheswaranathan, and Surya Ganguli. Deep unsupervised learning using nonequilibrium thermodynamics. In *ICML*, 2015. 2
- [41] Jiaming Song, Chenlin Meng, and Stefano Ermon. Denoising diffusion implicit models. *ICLR*, 2021. 2, 3
- [42] Yang Song, Jascha Sohl-Dickstein, Diederik P Kingma, Abhishek Kumar, Stefano Ermon, and Ben Poole. Score-based generative modeling through stochastic differential equations. *ICLR*, 2021. 2, 3
- [43] Charles M Stein. Estimation of the Mean of a Multivariate Normal Distribution. *The annals of Statistics*, 1981. 3
- [44] Lingchen Sun, Rongyuan Wu, Zhiyuan Ma, Shuaizheng Liu, Qiaosi Yi, and Lei Zhang. Pixel-level and semantic-level adjustable super-resolution: A dual-lora approach. 2025. 1, 2, 6, 7
- [45] Tencent Hunyuan3D Team. Hunyuan3d 2.0: Scaling diffusion models for high resolution textured 3d assets generation, 2025.
- [46] Tencent Hunyuan3D Team. Hunyuan3d 2.5: Towards high-fidelity 3d assets generation with ultimate details, 2025. 1
- [47] Narek Tumanyan, Michal Geyer, Shai Bagon, and Tali Dekel. Plug-and-play diffusion features for text-driven image-to-image translation. In *CVPR*, 2023. 2, 3
- [48] Ashish Vaswani, Noam Shazeer, Niki Parmar, Jakob Uszkoreit, Llion Jones, Aidan N Gomez, Łukasz Kaiser, and Illia Polosukhin. Attention is all you need. *NIPS*, 2017. 2, 6, 12

- [49] Jianyi Wang, Zongsheng Yue, Shangchen Zhou, Kelvin CK Chan, and Chen Change Loy. Exploiting diffusion prior for real-world image super-resolution. *IJCV*, 2024. 2
- [50] Yufei Wang, Wenhan Yang, Xinyuan Chen, Yaohui Wang, Lanqing Guo, Lap-Pui Chau, Ziwei Liu, Yu Qiao, Alex C Kot, and Bihan Wen. Sinsr: diffusion-based image superresolution in a single step. In CVPR, 2024.
- [51] Rongyuan Wu, Lingchen Sun, Zhiyuan Ma, and Lei Zhang. One-step effective diffusion network for real-world image super-resolution. *NeurIPS*, 2024.
- [52] Rongyuan Wu, Tao Yang, Lingchen Sun, Zhengqiang Zhang, Shuai Li, and Lei Zhang. Seesr: Towards semantics-aware real-world image super-resolution. In CVPR, 2024. 2
- [53] Wei Wu, Xi Guo, Weixuan Tang, Tingxuan Huang, Chiyu Wang, and Chenjing Ding. Drivescape: High-resolution driving video generation by multi-view feature fusion. In CVPR, 2025.
- [54] Guangxuan Xiao, Yuandong Tian, Beidi Chen, Song Han, and Mike Lewis. Efficient streaming language models with attention sinks. *ICLR*, 2024. 2
- [55] Fanghua Yu, Jinjin Gu, Zheyuan Li, Jinfan Hu, Xiangtao Kong, Xintao Wang, Jingwen He, Yu Qiao, and Chao Dong. Scaling up to excellence: Practicing model scaling for photorealistic image restoration in the wild. In CVPR, 2024. 2
- [56] Jinjin Zhang, Qiuyu Huang, Junjie Liu, Xiefan Guo, and Di Huang. Diffusion-4k: Ultra-high-resolution image synthesis with latent diffusion models. In CVPR, 2025. 1
- [57] Zechuan Zhang, Ji Xie, Yu Lu, Zongxin Yang, and Yi Yang. In-context edit: Enabling instructional image editing with in-context generation in large scale diffusion transformer. *NeurIPS*, 2025. 2
- [58] Tianrui Zhu, Shiyi Zhang, Jiawei Shao, and Yansong Tang. Kv-edit: Training-free image editing for precise background preservation. *ICCV*, 2025. 1, 2

Appendix

A. Pseudo-code of ScaleEdit

We provide an abstract overview of the proposed method by outlining its core procedure in Algorithm 1.

Algorithm 1 ScaleEdit

```
1: Inputs: Conditioning images I_{\text{src}}^{\text{high}}, I_{\text{src}}^{\text{low}}, I_{\text{ref}}^{\text{low}}, hyper-
        parameter \tau
       // 1. Forward process
 2: for i \leftarrow 1, \cdots, NM do
3: Get \{\mathbf{x}_t^{\text{high}}[i]\}_{t=0}^T, \{\mathbf{x}_t^{\text{low}}[i]\}_{t=0}^T, \{\mathbf{y}_t^{\text{low}}[i]\}_{t=0}^T
4: \tilde{\mathbf{x}}_T[i] \leftarrow \mathbf{x}_T^{\text{low}}[i], \tilde{\mathbf{y}}_T[i] \leftarrow \mathbf{y}_T^{\text{low}}[i]
  5: end for
       // 2. Transfer function optimization
  6: for t \leftarrow T, \cdots, 1, i \leftarrow 1, \cdots, NM do
               if t < \tau then
  8:
                        Optimize \phi_{\theta} using Eq. (6)
                        \Delta \mathbf{h}_t[i] \leftarrow \phi_{\theta}(\mathbf{h}_t[i], t)
  9:
 10:
                else
                       \Delta \mathbf{h}_t[i] \leftarrow \mathbf{0}
 11:
 12:
                Get \tilde{\mathbf{x}}_{t-1}[i] using Eq. (7)
 13:
 14: end for
        // 3. Detail injection with synchronization
15: for t \leftarrow T, \cdots, 1 do
                Get \tilde{\mathbf{y}}_{t-1}[i] using Eq. (9) for 1 \leq i \leq NM
 16:
                if t < \tau then
 17:
                        Get \tilde{\mathbf{y}}_t^{\text{rsp}}[i] using Eq. (13) for 1 \leq i \leq NM
 18:
19:
                       Get \tilde{\mathbf{y}}_{t-1}[i] using Eq. (14) for 1 \le i \le NM
20:
22: I_{\text{ref}}^{\text{high}} \leftarrow \text{Decode}(\text{Composite}(\{\tilde{\mathbf{y}}_0[i]\}_{i=1}^{NM}))
23: Output: Target image I_{\text{ref}}^{\text{high}}
```

B. Detailed explanation on synchronization

To synchronize adjacent patches, we introduce an auxiliary latent $\tilde{\mathbf{A}}_t[i,i+1]$, constructed by spatially blending the bottom half of $\tilde{\mathbf{y}}_t[i]$ and the upper half of $\tilde{\mathbf{y}}_t[i+1]$ at timestep t. Since each patch is denoised independently, their latent trajectories may diverge, often producing visible discontinuities along their boundary. However, $\tilde{\mathbf{A}}_t[i,i+1]$ contains the boundary region, and therefore its Tweedie estimate may naturally captures a smoother transition between the two patches. By blending the Tweedie estimate of an auxiliary patch with those of the original patches, the boundary between neighboring patches becomes more coherent, reducing artifacts and enhancing spatial continuity.

For the spatial blending, we first apply Eq. (2) to obtain

the original patches' Tweedie estimates:

$$\hat{\mathbf{x}}_{t\to 0}^{\text{aux}}[i,i+1] = \hat{\mathbf{x}}_0(\tilde{\mathbf{A}}_t[i,i+1],t)$$
(15)

$$\hat{\mathbf{x}}_{t\to 0}[i] = \hat{\mathbf{x}}_0(\tilde{\mathbf{y}}_t[i], t). \tag{16}$$

Then we define $L(\hat{\mathbf{x}}_{t\to 0}[i], \hat{\mathbf{x}}_{t\to 0}^{\mathrm{aux}}[i, i+1])$, a blended Tweedie estimate that is used to swap the $\hat{\mathbf{x}}_0$ term in Eq. (1) during the reverse process of $\tilde{\mathbf{y}}_t[i]$. Let \mathcal{T}_1 be the vertical translation operator defined in $[0, H_p] \times [0, W_p]$ as follows:

$$\mathcal{T}_1 f(u, v) = \begin{cases} 0, & 0 \le v < H_p/2, \\ f(u, v - H_p/2), & H_p/2 \le v \le H_p, \end{cases}$$
(17)

where W_p and H_p denote the patch width and height, respectively. Thus, $\mathcal{T}\hat{\mathbf{x}}_{t\to 0}^{\mathrm{aux}}[i]$ repositions $\hat{\mathbf{x}}_{t\to 0}^{\mathrm{aux}}[i]$ so that its top edge aligns with the midpoint of $\hat{\mathbf{x}}_{t\to 0}[i]$. Then we define a spatial weight mask $\mathbf{M}_1(u,v)$ for smooth transition across the overlap:

$$\mathbf{M}_{1}(u,v) = \begin{cases} 0, & 0 \le v < H_{p}/2, \\ \frac{v - H_{p}/2}{H_{p}/2}, & H_{p}/2 \le v \le H_{p}. \end{cases}$$
(18)

The blended Tweedie estimate is then computed as

$$L(\hat{\mathbf{x}}_{t\to 0}[i], \hat{\mathbf{x}}_{t\to 0}^{\mathrm{aux}}[i], \mathcal{T}_1)$$

$$= (1 - \mathbf{M}_1) \odot \hat{\mathbf{x}}_{t\to 0}[i] + \mathbf{M}_1 \odot \mathcal{T}_1 \hat{\mathbf{x}}_{t\to 0}^{\mathrm{aux}}[i]. \tag{19}$$

For the rest of the paragraph, we detail the case of $\tilde{\mathbf{y}}_t[i+1]$. Let \mathcal{T}_2 and $\mathbf{M}_2(u,v)$ defined in the vertically-flipped manner compared to \mathcal{T}_1 and $\mathbf{M}_1(u,v)$:

$$\mathcal{T}_2 f(u, v) = \begin{cases} f(u, v + H_p/2), & 0 \le v \le H_p/2\\ 0, & H_p/2 < v < H_p, \end{cases} (20)$$

$$\mathbf{M}_{2}(u,v) = \begin{cases} \frac{H_{p}/2 - v}{H_{p}/2}, & 0 \le v \le H_{p}/2\\ 0, & H_{p}/2 < v < H_{p}. \end{cases}$$
 (21)

Subsequently, the blended Tweedie estimate is formulated as:

$$L(\hat{\mathbf{x}}_{t\to 0}[i+1], \hat{\mathbf{x}}_{t\to 0}^{\text{aux}}[i+1], \mathcal{T}_2)$$

$$= (1 - \mathbf{M}_2) \odot \hat{\mathbf{x}}_{t\to 0}^{\text{aux}}[i+1] + \mathbf{M}_2 \odot \mathcal{T}_2 \hat{\mathbf{x}}_{t\to 0}^{\text{aux}}[i+1].$$
(22)

C. Implementation details

Latent decoding. After denoising $N \times M$ latent patches, we first merge them into a single latent tensor. The merged latent is then passed through the pretrained VAE decoder [22] to obtain the final high-resolution image $I_{\rm ref}^{\rm high}$.

Layer selection strategy. We describe how we select the layers of the pretrained generative models to which the detail enhancement module is attached. For Stable Diffusion [37], the U-Net [38] decoder contains four upsampling blocks,

each composed of three sub-blocks. We insert a 1×1 convolution layer into the last sub-block of each upsampling block, resulting in four additional 1×1 convolution layers in total. For FLUX [23], we attach the detail enhancement module to the linear layer located immediately after the last single-stream block, which is a layer followed by a Layer Normalization operation.

D. Additional ablation studies

Impact of hyperparameter τ . As described in Algorithm 1, ScaleEdit utilizes a hyperparameter τ . To investigate its effect, we conduct an ablation study by varying τ in 15, 25, 35 and evaluate the results using the same metrics as the main experiment on a set of 60 (image, instruction) pairs. As shown in Tab. 2, the default setting $\tau=35$ achieves the best performance across all metrics.

Table 2. Ablation study on τ values.

$\overline{\tau}$	HaarPSI	M-MSE	M-SSIM	M-PSNR
15	0.332	0.056	<u>0.749</u>	22.844
25	0.327	0.056	0.753	22.890
35	0.335	0.056	0.761	23.172

Ablation on synchronization strategy. In Figure 7, we illustrate the effect of the proposed synchronization method. As shown, naive patch sampling without synchronization brings noticeable edge artifacts along patch boundaries, whereas our method effectively mitigates these artifacts.

E. Receptive field of diffusion models

In this work, we leverage a low-resolution image generation model to perform high-resolution image editing in a patch-wise manner. Although FreeScale [35] modifies internal components of a low-resolution diffusion model (*e.g.*, via dilated convolutions) to generate high-resolution outputs, such architectural changes do not guarantee a strong high-resolution image prior, as the model is not trained on high-resolution image datasets.

In contrast, our patch-wise approach is well-suited for extracting detailed information. Each patch matches the resolution of the low-resolution model's receptive field ($e.g.512 \times 512$ for the pretrained Stable Diffusion [37]), enabling faithful detail reconstruction without modifying the underlying generator. The main challenge in the modified framework lies in generating details that the model was not originally trained to produce. For these reasons, we adopt a patch-wise strategy grounded in low-resolution image priors instead of modifying diffusion architectures to synthesize high-resolution content directly.



Figure 6. [Best visualized when magnified.] We visualize the results of our method combined with the pretrained FLUX 1-dev [23] model.

F. Additional qualitative results

We show the additional results of ScaleEdit in Figure 6 and 8. Figure 6 shows that our method is even applicable to transformer-based [48] FLUX model [23], demonstrating the robustness and generalizability of our method across backbone architectures. Then, we show the additional 1K-and 2K-editing results obtained with the pretrained Stable Diffusion [37] in Figure 8. We emphasize that the proposed method effectively transfers the fine-grained details of the source image into the target image.

G. Limitations

Our method may produce suboptimal results due to the limited performance of the pretrained generative models [23, 37]. Furthermore, since the proposed method relies on the low-resolution reference image $I_{\rm ref}^{\rm low}$ generated by existing low-resolution image-to-image translation methods [14], some artifacts introduced by these editing methods can propagate to the final high-resolution output $I_{\rm ref}^{\rm high}$, potentially leading to visible artifacts.

H. Societal impacts

The proposed method may generate some harmful images due to the imperfections of the underlying pretrained generative models [23, 37]. Rare cases of undesired or inappropriate results may arise, especially when the generative prior itself produces such outputs under challenging conditions.

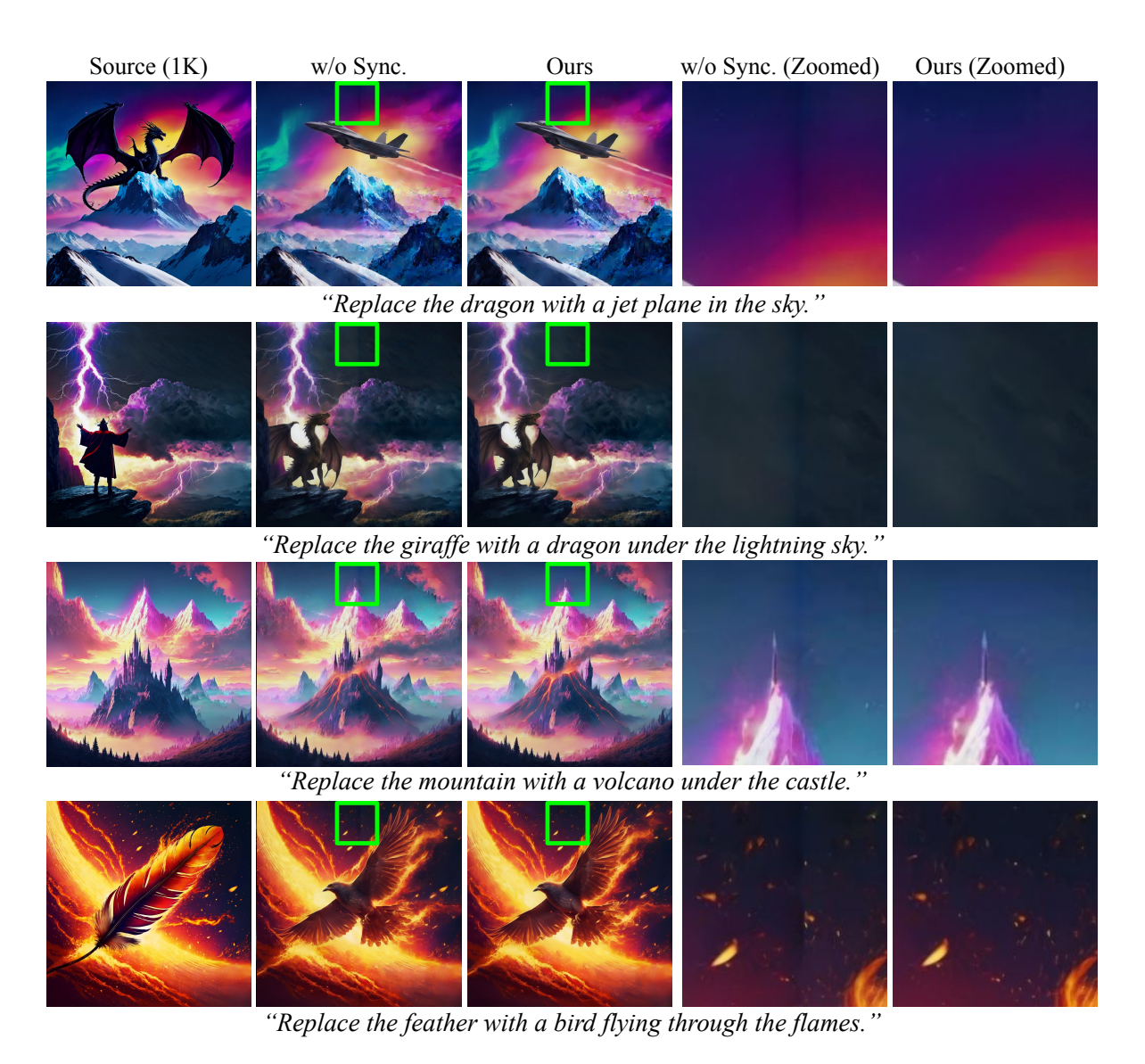


Figure 7. **[Best visualized when magnified.]** Effectiveness of the proposed synchronization strategy. While images sampled without synchronization incorporates a significant artifact on the patch boundaries, our method effectively alleviates the edge artifacts.

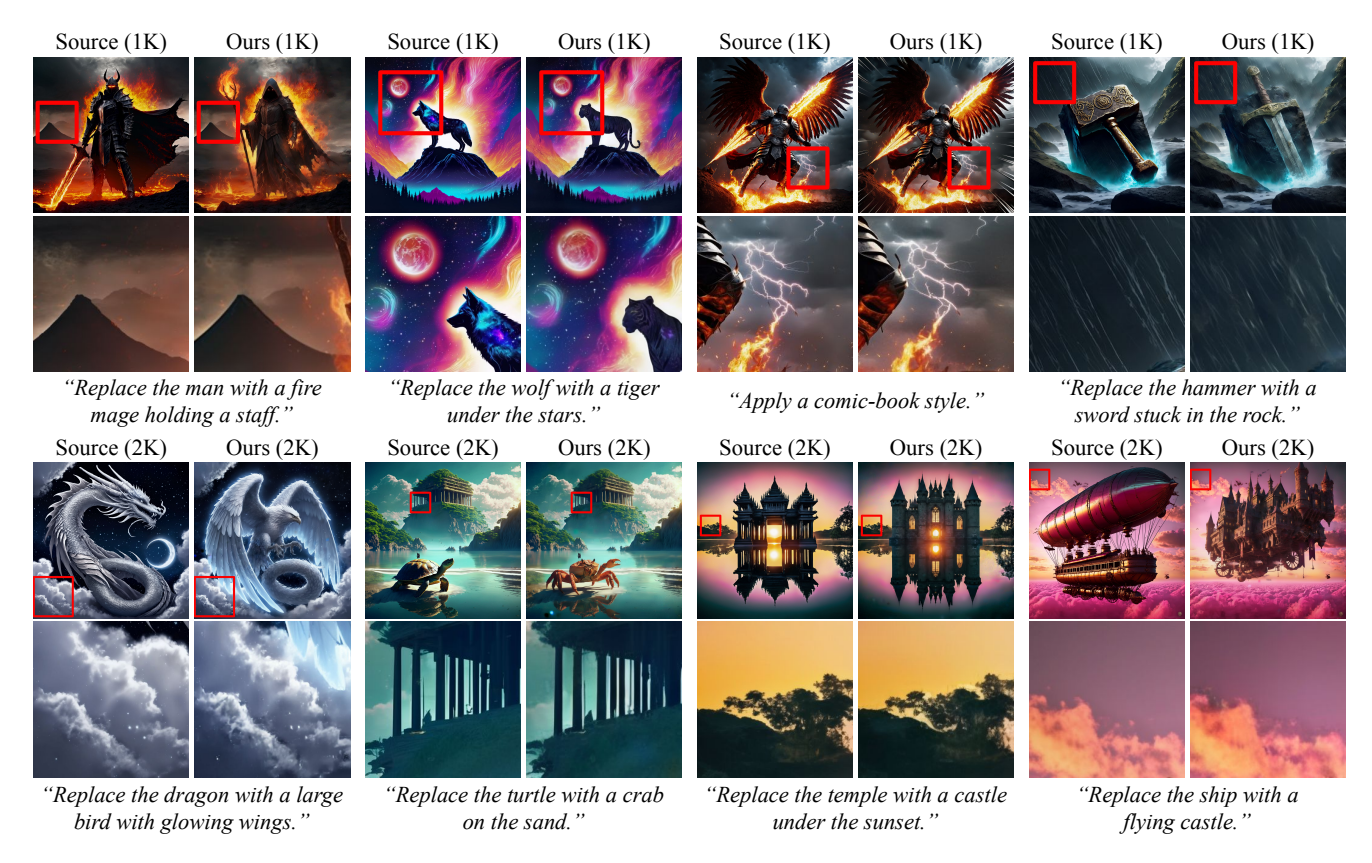


Figure 8. **[Best visualized when magnified.]** We visualize the additional results of 1K-editing and 2K-editing. By conditioning on low-resolution reference images, our method is successfully synthesizes high-resolution edited images.